Gyrokinetic δf particle simulations of toroidicity-induced Alfvén eigenmode

Jianying Lang,[1,a)] Yang Chen,[1] Scott E. Parker,[1] and Guo-Yong Fu[2]
[1]*University of Colorado at Boulder, Boulder, Colorado 80309, USA*
[2]*Princeton Plasma Physics Laboratory, Princeton, New Jersey 08543, USA*

(Received 22 June 2009; accepted 14 September 2009; published online 7 October 2009)

Gyrokinetic δf particle simulation is used to investigate toroidicity-induced Alfvén eigenmodes (TAEs). Both thermal ions and energetic particles are fully kinetic, but a reduced fluid model is used for the electrons. Simulation of a single $n=2$ global TAE is carefully analyzed and benchmarked with an eigenmode analysis, and a very good agreement is achieved in both mode structure and mode frequency. The instability of the mode in the presence of energetic particles is demonstrated. In particular, gyrokinetic simulations demonstrate the kinetic damping effect of thermal ions, where the finite radial structure of kinetic Alfvén waves is well resolved and the damping rate is compared to and found to agree well with analytical theory. © *2009 American Institute of Physics*. [doi:10.1063/1.3243493]

I. INTRODUCTION

As the ignition condition for tokamak plasmas is approached, alpha particles produced by D-T reactions and other suprathermal ions, such as that produced in ion cyclotron range of frequency heating and neutral beam injection, will form a significant fraction of the total plasma pressure. These energetic particles can resonantly excite shear Alfvén instabilities such as toroidal-induced Alfvén eigenmodes (TAE)[1–3] and energetic particle-driven mode (EPM)[4,5] or resonant TAE.[6] Most previous numerical studies are based on the kinetic-magnetohydrodynamics (MHD) model, where the energetic species is described by gyrokinetics, while the background plasma is described by a MHD model.[7–10] The hybrid model is suitable for large scale instabilities such TAEs. However, the kinetic-MHD hybrid model fails to capture the full kinetic physics. For example, Landau damping as an important kinetic resonance is neglected. Also neglected are the thermal ion finite Larmor radius (FLR) effects and the parallel electric field $E_{\parallel}=-\nabla_{\parallel}\delta P_e/en_0$ due to electron pressure δP_e. To include the kinetic effects of both the energetic particles and thermal ions, a fully kinetic model is required. The kinetic effects of thermal species are essential for retaining the important background damping of the shear Alfvén waves as well as for the ion temperature gradient-driven Alfvén instabilities.[11]

Recently, a number of gyrokinetic global codes[12–16] have been developed to simulate low-n TAEs. Lauber *et al.*[12,13] employed gyrokinetic model of MHD modes[17,18] in their global gyrokinetic eigenvalue code, whereas Nishimura *et al.*[14,15] and Mishchenko *et al.*[16] took the gyrokinetic δf particle-in-cell approach. Applying similar model as in Refs. 14–16, we use a global gyrokinetic δf particle code—GEM—to simulate a single TAE. GEM was originally developed as a flux-tube code[19] and was later extended to include global geometry and arbitrary equilibrium profiles.[20] GEM includes fully kinetic ions and electrons. We have attempted to use GEM, with kinetic electrons, to study low-n TAE modes directly. It turns out that in order to accurately solve the "cancellation problem"[21] for long wavelength modes, more particles and finer spatial grids need to be used. This is counterintuitive since one expects to use fewer particles and coarser grids for low-n modes. We therefore have implemented the massless fluid electron model[22] in GEM. The fluid electron model consists of an electron continuity equation, a parallel Ohm's law, and a closure equation for the electron temperature. This model can be reduced to the exact MHD eigenmode equation when electron pressure is neglected in Ohm's law, making a direct comparison with MHD results possible. Both energetic particles and core thermal ions are fully gyrokinetic. Compared to the usual kinetic-MHD hybrid model, the gyrokinetic model used in this work has more physics in terms of thermal ion kinetic effects and parallel electric field due to electron pressure.

For high-n drift-wave simulations, the use of the field-line-following coordinates, together with some approximations made to the final field equations expressed in the field-line-coordinates, significantly improves the computational efficiency. For instance, one of the approximations made in Ampere's equation is that only second-order derivatives in the coordinates (x,y), which label the field line, need to be retained for the differential operator. It is not *a priori* clear whether such approximations are valid for low-n modes. In this work, an eigenmode analysis of the basic fluid equations is carried out as a validation for the simulation model. Comparison of the simulation results with the eigenmode analysis shows that the usual algorithm for the field equations is sufficiently accurate. To accurately characterize TAE instabilities, one important issue is to study the kinetic damping effects, of which the "radiative" damping[23,24] due to coupling to the kinetic Alfvén waves (KAWs)[25] is of particular interest. Using fully kinetic treatment of both energetic particles and thermal ions, we observe the mode conversion from TAEs to KAWs, which results in the radiative damping. We also quantitatively characterize the kinetic damping rate and compare it to theoretical calculations.

[a)]Present address: Princeton Plasma Physics Laboratory, Princeton, NJ 08543.

This paper is organized as follows. In Sec. II, we summarize the simulation model used in this work. In Sec. III, we benchmark our simulation results from a reduced model with an eigenmode analysis. In Sec. IV, we show that the TAE is driven unstable in the presence of energetic particles. In Sec. V, we present simulation results of the kinetic radiative damping. Further details for the eigenmode analysis are given in the Appendix.

II. SIMULATION MODEL

The hybrid model containing fully gyrokinetic ions and zero-inertia electrons, which are described in detail in Refs. 20 and 22, will only be briefly summarized here.

A. Massless fluid electron

First, we briefly summarize the fluid electron model that replaces the kinetic electrons in the GEM code. Kinetic electrons in GEM code have turned out to be working very well at finite plasma β in turbulence simulations.[19,20] However, kinetic electron model becomes more numerically challenging at large plasma β for long wavelength modes. In this work, we employ zero-inertia electrons to obtain the electron parallel current, which circumvents numerical difficulties such as time step constraint on $k_\parallel v_{T_e}\Delta t$ and electron free streaming noise.

Massless electron assumption gives $m_e \to 0$ and keeps finite electron temperature T_e. This assumption neglects the effects of trapped electrons but retains passing electrons, which are the main contributors to the parallel current. Electron continuity equation is derived by taking velocity space moments of the drift kinetic equation by neglecting electron density gradient

$$\frac{\partial \delta n_e}{\partial t} + \mathbf{B}\cdot\nabla\frac{n_0 u_{\parallel e}}{B} + \frac{1}{B^3}\mathbf{B}\times\nabla B\cdot\nabla\delta P_e + \frac{2n_0}{B^3}\mathbf{B} \times \nabla B\cdot\nabla\delta\phi = 0. \tag{1}$$

Here, n_0 is the background plasma density and the operator $\nabla_\parallel$ is defined along the magnetic field line $\nabla_\parallel = \mathbf{b}\cdot\nabla$. The perturbed electron pressure is defined by $\delta P_e = \delta n_e T_e$, where δn_e is the perturbed electron density and T_e is the electron temperature.

The form of Ohm's law employed in simulations is

$$en_0 E_\parallel = -\mathbf{b}\cdot\nabla\delta P_e, \tag{2}$$

and the vector potential is given by

$$\frac{\partial \delta A_\parallel}{\partial t} = -\mathbf{b}\cdot\nabla\delta\phi - E_\parallel. \tag{3}$$

More details about the equations can be found in Ref. 22 and references therein.

B. Gyrokinetic ions

In the simulation, we apply the same set of gyrokinetic equations to both energetic particles and thermal ions. The distribution function of kinetic ions is separated into an equilibrium part f_{i0} and a perturbed part δf_i. The gyrokinetic equation is

$$\frac{d\delta f_i}{dt} = -\left(v_\parallel\frac{\langle\delta\mathbf{B}_\perp\rangle}{B} + \langle\mathbf{v}_\mathbf{E}\rangle\right)\cdot\nabla f_{i0} + \frac{\dot{\varepsilon}_i}{T_\alpha}f_{i0}, \tag{4}$$

where

$$\dot{v}_\parallel = -\frac{\mu}{m_i}\mathbf{b}\cdot\nabla B,$$
$$\dot{\varepsilon}_i = \dot{x}E_x + \dot{y}E_y + \dot{z}E_z. \tag{5}$$

Here, $v_\parallel$ is the parallel drift along the magnetic field direction, $\langle\mathbf{v}_\mathbf{E}\rangle$ is evaluated as $\langle\mathbf{E}\rangle\times\mathbf{b}/B$, and $\varepsilon_i = 1/2 m_i(v_\perp^2 + v_\parallel^2)$ is the particle kinetic energy. The perpendicular electric field $\mathbf{E}_\perp$ is computed from the perturbed electric potential $\delta\phi$ and the parallel electric field $\mathbf{E}_\parallel$ is computed from the perturbed electron pressure δP_e according to Ohm's law. That is, $E_x = -\partial\delta\phi/\partial x$, $E_y = -\partial\delta\phi/\partial y$, and $E_\parallel = -\nabla_\parallel\delta P_e/en_0$. The ion equilibrium distribution function is defined by

$$(v_\parallel\tilde{\mathbf{b}} + \mathbf{v}_D + \mathbf{v}_{E0})\cdot\nabla f_{i0} = 0, \tag{6}$$

where $\tilde{\mathbf{b}} = \mathbf{b} + \delta\mathbf{B}_\perp/B$, $\mathbf{v}_E = \langle E\rangle\times\mathbf{b}/B$, and $\mathbf{v}_D = m_i(v_\parallel^2 + v_\perp^2/2)/qB^3(\mathbf{B}\times\nabla B)$ is the grad B and curvature drift velocity. Gyroaveraging is done as usual with the four-point averaging scheme[26] where numerical details are described in Ref. 20.

In simulations, the perturbed part δf is represented by particle weight $w_j = \delta f/f_{i0}$, and the weight evolves according to

$$\frac{dw_j}{dt} = -\left(v_\parallel\frac{\delta\mathbf{B}_\perp}{B} + \mathbf{v}_\mathbf{E}\right)\cdot\frac{1}{f_{i0}}\nabla f_{i0} + \frac{\dot{\varepsilon}_i}{T_i}, \tag{7}$$

where w_j is the weight of the jth particle. The particle coordinates evolve according to the following equations:

$$\dot{x} = \frac{m_i v_\parallel^2 + \mu B}{eB^3}\mathbf{B}\times\nabla B\cdot\nabla x + \frac{1}{B}\left(-\frac{\partial\delta\phi}{\partial y} + v_\parallel\frac{\delta B_x}{B}\right)\mathbf{b}\cdot\nabla x \times\nabla y,$$
$$\dot{y} = \frac{m_i v_\parallel^2 + \mu B}{eB^3}\mathbf{B}\times\nabla B\cdot\nabla y + \frac{1}{B}\left(\frac{\partial\delta\phi}{\partial x} + v_\parallel\frac{\delta B_y}{B}\right)\mathbf{b}\cdot\nabla x \times\nabla y, \tag{8}$$
$$\dot{z} = \frac{m_i v_\parallel^2 + \mu B}{eB^3}\nabla z\cdot\mathbf{B}\times\nabla B + v_\parallel\mathbf{b}\cdot\nabla z,$$

where the magnetic moment $\mu = m_i v_\perp^2/2B$ is an adiabatic invariant. From the time evolution of coordinates, velocity, and weight, we can obtain the information $(\mathbf{x}_j, \mathbf{v}_j, w_j)$ on each particle at every time step. The particle information will give the perturbed ion density and current in real space by

$$\delta n(\mathbf{x}) = \int \delta f(\mathbf{x},\mathbf{v})d^3v \quad \text{and} \quad \delta j_\parallel(\mathbf{x}) = \int \delta f(\mathbf{x},\mathbf{v})v_\parallel d^3v. \tag{9}$$

Numerically, the perturbed density and current at each grid

point are computed by summation over particles near the grid point instead of an integral. In the summation, the Jacobian $J=(\nabla x\cdot\nabla y\times\nabla z)^{-1}$ induced by the coordinate transformation should be considered. Zero boundary conditions are applied and ions that hit the radial boundaries are put back in the simulation domain at the other side of the midplane where their unperturbed trajectories intersect the radial boundaries. More details for gyrokinetic ions can be found in Ref. 20 and references therein.

Gyrokinetic Poisson equation is used to solve for the perturbed electric potential from the perturbed density

$$\sum_k [1-\Gamma_0(b)e^{i\mathbf{k}\cdot\mathbf{x}}]\phi_k = \delta n_i + \delta n_\alpha - \delta n_e, \tag{10}$$

where $b=k_\perp^2\rho_i^2$, ρ_i is the normalized length unit, $\rho_i=\sqrt{m_pT_p}/eB_0$, where m_p is the proton mass, T_p is a temperature normalization, and B_0 is a magnetic field normalization. The magnetic field $B(r,\theta)$ contains the real space dependence and is evaluated from the equilibrium profile in toroidal coordinates. Here, Miller equilibrium profiles are applied.[27] In simulations, the three-dimensional (3D) equation [Eq. (10)] is solved by converting the left-hand side operator to a matrix using a pseudospectrum method (see details in Ref. 20). Energetic particles (δn_α), thermal ions (δn_i), and electrons (δn_e) are taken into account through perturbed density on the right-hand side of Eq. (14). The perturbed energetic particle and core thermal ion density are computed from the perturbed distribution function, and the electron perturbed density is obtained from the electron fluid equation.

III. COMPARISONS BETWEEN SIMULATION RESULTS AND EIGENMODE ANALYSIS

As the first step to validate our code, we reduce simulation model in order to directly compare to an eigenmode calculation. Neglecting electron and ion pressure term, the total charge continuity equation and Ohm's law can be simplified at low beta as

$$\frac{\partial}{\partial t}(\delta n_i - \delta n_e) + \mathbf{B}\cdot\nabla\frac{n_0(\delta u_{\parallel i}-\delta u_{\parallel e})}{B} = 0, \tag{11}$$

$$\frac{\partial \delta A_\parallel}{\partial t} + \mathbf{b}\cdot\nabla\delta\phi = 0, \tag{12}$$

where $\mathbf{b}=\mathbf{B}/B$ indicates the magnetic field direction and $\delta u_{\parallel\alpha}$ ($\alpha=i,e$) is the perturbed parallel velocity, which is given by Ampere's law

$$-\nabla_\perp^2\delta A_\parallel = \mu_0 e n_0(\delta u_{\parallel i}-\delta u_{\parallel e}). \tag{13}$$

To make benchmark, we take long the wavelength limit of the gyrokinetic Poisson equation, which gives

$$-\nabla\cdot\frac{n_0m_i}{B(r,\theta)^2}\nabla_\perp\delta\phi = \delta n_\alpha + \delta n_i - \delta n_e. \tag{14}$$

Ignoring kinetic effects of ions (both the energetic particles and thermal ions) in gyrokinetic Poisson equation [Eq. (14)] and combining with Ampere's law, the simplified charge continuity equation, and Ohm's law (simplified as Faraday's law), one can obtain the MHD eigenequation for TAEs

$$\frac{\partial^2}{\partial t^2}\nabla\cdot\frac{1}{V_A(r)^2}\nabla_\perp\delta\phi = \mathbf{B}\cdot\nabla\frac{1}{B}\nabla_\perp^2\mathbf{b}\cdot\nabla\delta\phi. \tag{15}$$

Here, $v_A=B/(4\pi n_0m_i)^{1/2}$ is the Alfvén speed. Solving for the eigenvalues and the eigenfunctions of Eq. (15), one can get the corresponding eigenfrequencies and the mode structure of TAEs (details are shown in the Appendix). In toroidal geometry, the mode structure (electrostatic potential) is a function of the radial position r, the toroidal position ζ, and the poloidal position θ. It can generally be described by a Fourier decomposition in poloidal harmonics as

$$\delta\phi(r,\theta,\zeta,t) = \sum_m \delta\phi_m(r)\exp(-im\theta+in\zeta-i\omega t), \tag{16}$$

where m and n are the poloidal and toroidal mode numbers, and n is a good quantum number. The mode frequency is determined by the breaking of shear Alfvén continuum spectra. For a given toroidal number n, the interaction between adjacent poloidal harmonics of Alfvén waves causes a frequency gap in the continuous spectra. The radial position r corresponding to a frequency gap is determined by the safety factor profile and toroidal/poloidal mode numbers $q(r)=(m+1/2)/n$. The gap frequency range is bounded by the formula[2]

$$\omega_\pm = \frac{k_{\parallel m}^2v_A^2+k_{\parallel m+1}^2v_A^2 \pm \sqrt{(k_{\parallel m}^2v_A^2+k_{\parallel m+1}^2v_A^2)^2+4\epsilon^2x^2k_{\parallel m}^2v_A^2k_{\parallel m+1}^2v_A^2}}{2(1-\epsilon^2x^2)}, \tag{17}$$

where $k_{\parallel m}=(n-m/q)/R$ is the parallel wavenumber, $x=r/a$ is the normalized radius, and $\epsilon=\Delta'/x+a/R$ indicates the coupling strength of poloidal harmonics. ϵ is of the same order as the inverse aspect ratio and Δ' is derived from the Shafranov shift.[28,29] The gap size at the crossing point is $\Delta\omega=\omega_+-\omega_-\simeq 2\epsilon x|k_{\parallel m}v_A|$. In the limit of $\epsilon=0$, the poloidal harmonics are uncoupled, which gives the continuum solution $\omega_m=k_{\parallel m}V_A$.

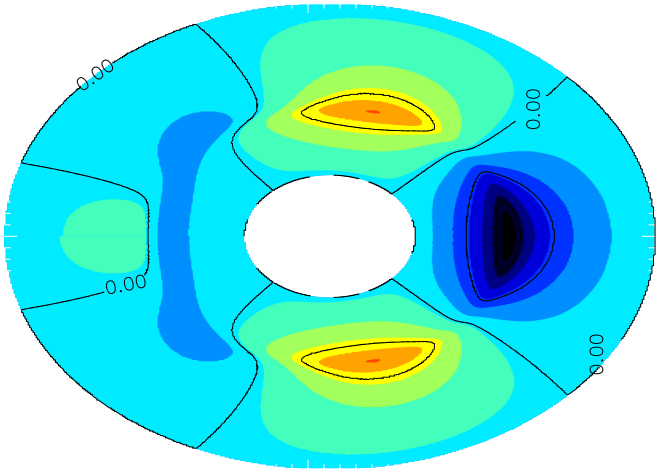

FIG. 1. (Color online) The contour plot of the electric potential in the R-θ plane for $n=2$ mode obtained from eigenmode calculations.

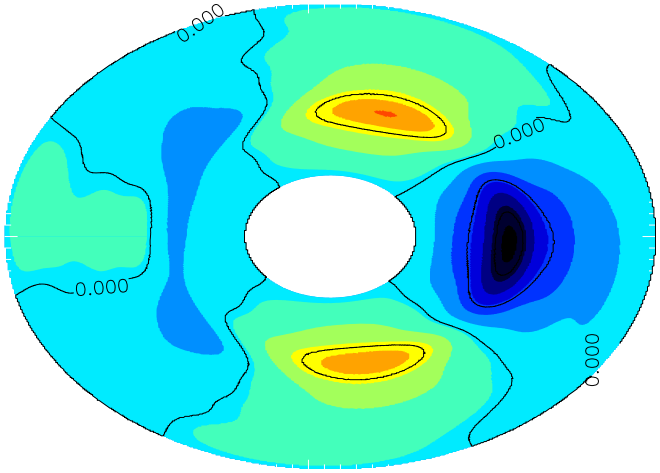

FIG. 3. (Color online) The contour plot of the electric potential in the R-θ plane for $n=2$ mode obtained from reduced model simulation.

The physical parameters used in the eigenmode analysis are the same as those used in simulations. Throughout this paper we study a single $n=2$ global TAE mode.

A. Eigenmode analysis

We employ a simple analytical equilibrium profile. This is done by specifying simple profiles that define the Miller equilibrium, i.e., setting the elongation profile $\kappa(r)=1$ and triangulation $\delta(r)=0$. For simplicity, the major radius R_{maj} is set constant so that the Shafranov shift is eliminated. The equilibrium magnetic flux surface becomes circular concentric. The major radius is $R_{\mathrm{maj}}=713.7\rho_i$ and the minor radius is $128.46\rho_i$. We take safety factor profile as $q(r)=q_0(r/r_0)^{0.3}$, where $q_0=1.3$ is the safety factor at $r=R_0$. Note that the safety factor becomes less than 1 at the inner edge, which will excite current-driven MHD instabilities. To avoid possible instabilities, we set the radial simulation regime $[0.2a, 0.8a]$, where $a=2r_0$ and zero-boundary condition is applied. The magnetic shear at $r=r_0$ is $\hat{s}=0.3$ and the plasma to magnetic pressure ratio is $\beta(r,\theta)=0.3\%(1+0.18\cos\theta)^2$. The plasma temperature is set constant $T_i=T_e=T_p$ and the thermal ion mass is $m_i=2m_p$. These physical parameters will determine the number of TAEs in the continuum gap, their frequencies, and their mode structures. The $n=2$ mode studied here corresponds to the fundamental mode in y with a box size of $L_y=310.44\rho_i$. Other numerical parameters used in simulations are as follows: the grid numbers in field-line-following coordinates are $N_x=128$, $N_y=32$, and $N_z=32$; the time step is $\omega_{ci}\Delta t=2.0$. N_y is small since only the fundamental mode is to be resolved.

Because of the presence of many grid-scale modes, eigenmode analysis yields thousands of modes using the above parameters. Among them, we pick out the desired TAE mode. The mode frequency is identical to that in the simulation results (which will be shown in Sec. III B). The corresponding eigenfunction is also very close to the TAE mode structure obtained from simulations. Figure 1 shows the electric potential contour plot (in the R-θ plane) from eigenmode analysis.

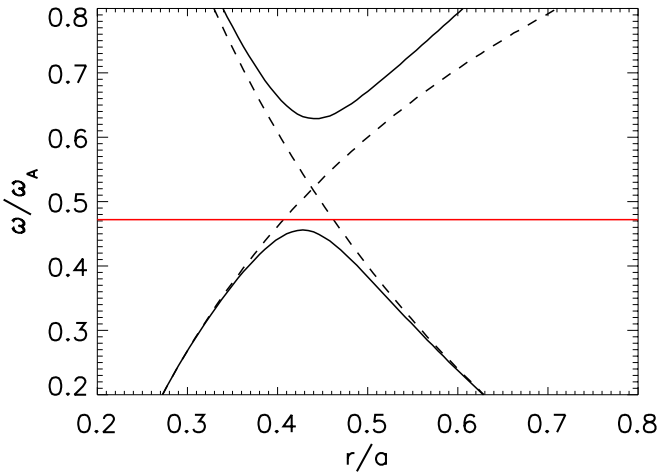

FIG. 2. (Color online) The spectrum of toroidal shear Alfvén continuous spectra (curved solid line) obtained from analytical calculations with the TAE (straight solid line) obtained from simulations; the cylindrical (dashed lines) spectra for $m=2$ and $m=3$ with $n=2$ from analytical calculations.

B. Simulation results

In the simulation the perturbed electron density and the vector potential are evolved in time using an explicit method. The electrostatic potential is computed from the quasineutrality condition (gyrokinetic Poisson equation [Eq. (14)]). Once $\delta A_\parallel$ is known, the electron flow velocity $u_\parallel$ is computed using Ampere's equation. For benchmarking purpose, the same approximations (see detail in the Appendix) made in the eigenmode analysis are made in the simulations.

From the time evolution of the electric potential for the same $n=2$ mode, we obtain the mode frequency $\omega\simeq 0.472V_A/q_0R$. Compared to the MHD theory prediction of the continuum gap, this mode (the solid line) is well within the gap, as shown in Fig. 2. In the frequency spectrum, the mode is closer to the lower continuum. This is expected because the magnetic shear $\hat{s}\leq 0.3$ is low. The contour plot of the electric potential in the R-θ plane is shown in Fig. 3. From this plot, we can see the two-dimensional mode

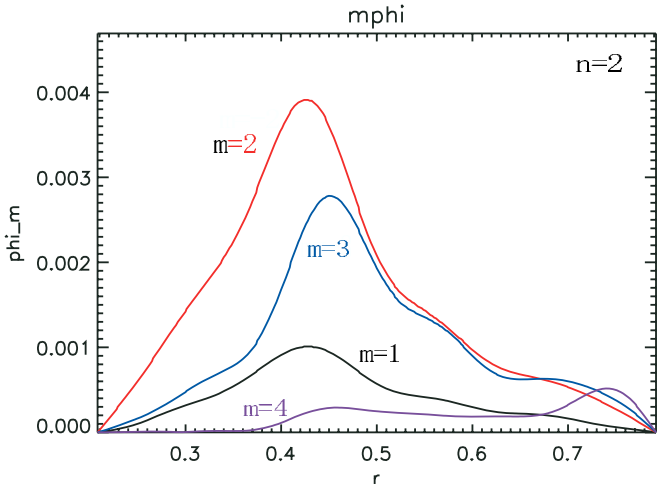

FIG. 4. (Color online) Radial profile of different poloidal harmonics for the $n=2$ mode; from top to bottom, the first line is for $m=2$, the second line is for $m=3$, the third line is for $m=1$, and the fourth line is for $m=4$. This is from the reduced model simulation.

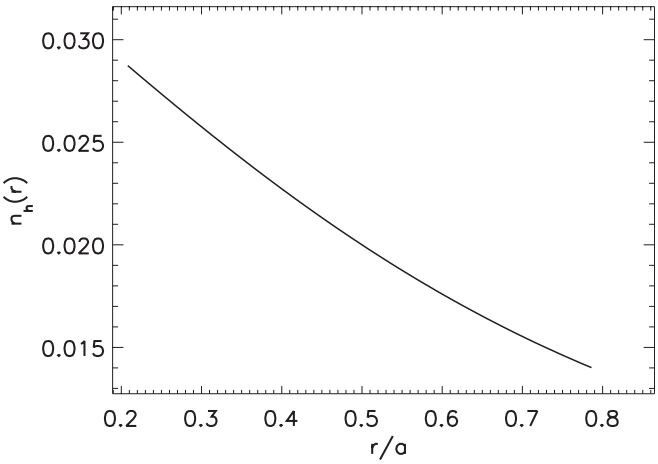

FIG. 5. The radial profile of the energetic particle density; the radial simulation domain is from $0.2a$ to $0.8a$.

structure in a poloidal cross section. It clearly shows the radial position of the mode and the shape.

Compared to eigenmode calculation shown in Fig. 1, the electric potential contour shows very good agreement in both the mode shape and the mode location. Agreement among the eigenmode analysis, the simulations, and the theoretical calculation confirms that the mode obtained from the simulation is a TAE. To more clearly see different poloidal harmonics, we view the mode structure in the radial direction for fixed toroidal mode number $n=2$. Figure 4 shows the radial variation in different poloidal harmonics. We see that the poloidal harmonics $m=2$ and $m=3$ dominate over other modes.

IV. ENERGETIC-PARTICLE-DRIVEN TOROIDICITY-INDUCED ALFVÉN EIGENMODES

Based on the TAE mode ($n=2$) obtained from the reduced model simulation, we now self-consistently turn on energetic particles, thermal kinetic ions, and electron pressure term. Both energetic particles and thermal ion are treated as fully gyrokinetic as described Sec. III B, which are included in the right-hand side of Eq. (14), whereas electrons are with treated as massless fluid [Eq. (1)]. Electron pressure term is calculated in Eq. (2) and is taken into account through Eq. (3).

The ion (both energetic particles and core thermal ions) distribution in velocity is assumed to be Maxwellian with a flat temperature profile. The parameters and profiles for the energetic particles are as follows: the temperature is $T_h=300T_p$ (T_p is a virtual temperature unit) and the hot particle density is

$$n_h(r) = 0.02n_0 e^{-1.156\ \tanh(r/a-0.5)/0.9} \tag{18}$$

(n_0 is the background plasma density, which is set to unity). This density profile is shown in Fig. 5, where the central hot plasma pressure is $\beta_h(0)=1.8\%$. The analytical form of the safety factor profile is $q(r)=1.3(r/r_0)^{0.3}$, which is shown in Fig. 6. The energetic particle number per grid cell is 16. Core thermal ions are uniform in real space with a constant temperature $T_i=T_p$, and the particle number per grid cell is also 16.

Using the above listed parameters and those in Sec. III A, the single TAE mode ($n=2$) is destabilized. The time evolution of this mode is shown in Fig. 7, which exhibits the real part of the electrostatic potential after a Fourier transform along the radial and field-line directions with only the dominant radial wavenumber retained. The mode frequency has changed within 2% compared to that obtained from reduced model simulations. The radial profiles of different poloidal harmonics are shown in Fig. 8, which shows that the harmonic $m=2$ is clearly dominant, consistent with simulation results from reduced model. Figure 9 shows the snapshot of electric potential contour plot in the R-θ plane. Compared to Fig. 3 obtained from reduced model simulation, the mode has the same radial position but rotates along poloidal direction which is expected as well.

Varying the energetic particle central pressure $\beta_h(0)$ by changing the central energetic particle density $n_h(0)$, we ob-

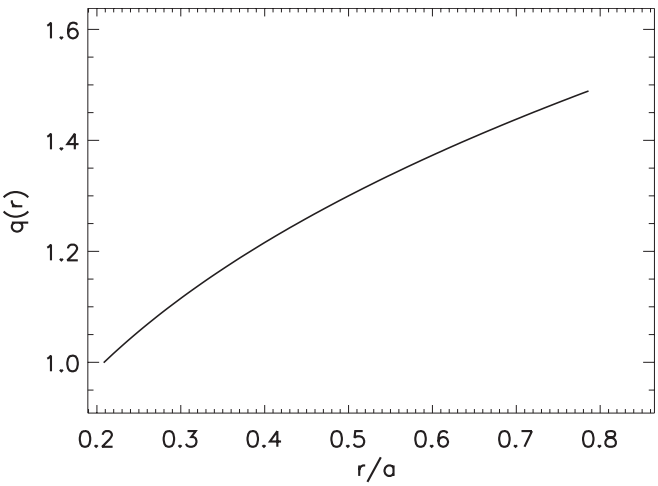

FIG. 6. The radial profile of the safety factor; the radial simulation domain is from $0.2a$ to $0.8a$.

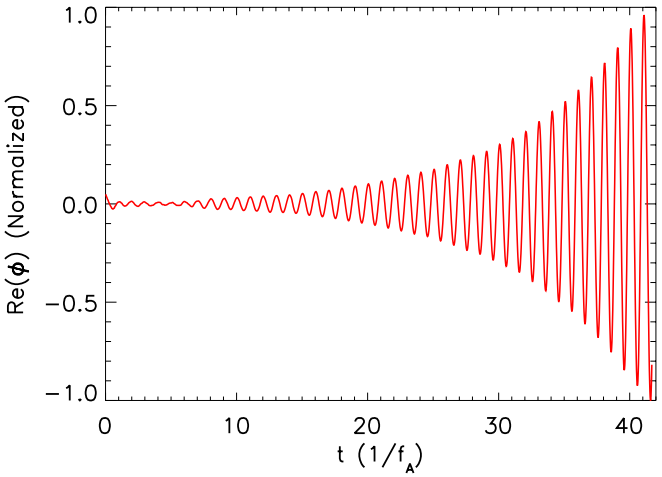

FIG. 7. (Color online) The time evolution of the mode's electric potential $\delta\phi(k_x=0,k_y=2\pi/L_y,k_z=0)$. The electric potential is normalized with the maximum value in this time regime. This is obtained from simulations with kinetic energetic particles and thermal ions.

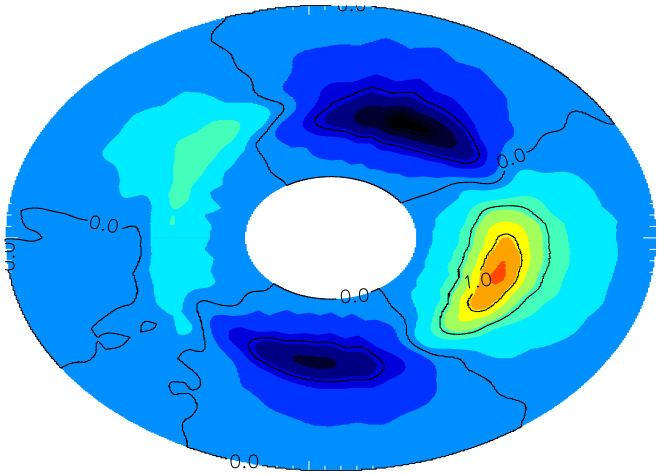

FIG. 9. (Color online) The contour plot of the electric potential in the R-θ plane for $n=2$ mode obtained from simulations with kinetic energetic particles, kinetic thermal ions, and electron pressure term all included.

serve a near-linear scaling between the normalized mode growth rate γ/ω and $\beta_h(0)$, where ω indicates the mode frequency. Figure 10(a) shows the growth rate versus central energetic particle pressure. The scaling of growth rate with β_h is easy to understand because energetic particles are the driving source. Figure 10(b) shows that the mode frequency slightly decreases with the increase in the central energetic particle pressure but the whole range of frequency variation is within 2%. For future work, we could further increase the energetic particle pressure and investigate the transition from TAEs to energetic particle continuum modes.[30]

For comparison, we also carry out simulations using the conventional hybrid approach. We now only take into account the gyrokinetic effects of energetic particles in Eq. (14), whereas the background plasmas are treated using the reduced model, that is, Eqs. (12) and (13).

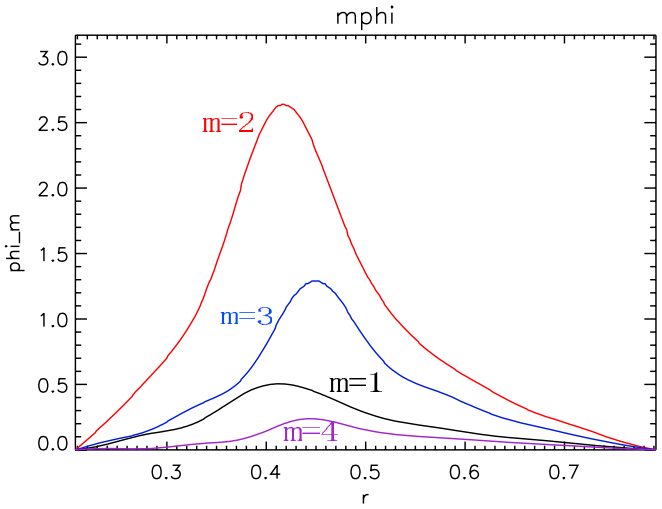

FIG. 8. (Color online) Radial profile of different poloidal harmonics for the $n=2$ mode in the presence of energetic particle drive; from top to bottom, the first line is for $m=2$, the second line is for $m=3$, the third line is for $m=1$, and the fourth line is for $m=4$ (from simulations). This is from simulations with kinetic energetic particles and thermal ions.

We first check the radial structure of different poloidal harmonics, as shown in Fig. 11. Compared to Fig. 8 obtained in simulations with kinetic thermal ions, they are nearly identical. The scaling of linear growth rate and mode frequency versus energetic particle pressure β_{hot} is shown in Fig. 12. In Fig. 12(a), the solid line indicates the mode growth rate with energetic particle FLR effect, whereas the dashed line does not include that effect. Figure 12(b) shows the mode frequency versus central energetic particle pressure in the presence of energetic particle FLR effect. From the plot, we can see that the mode frequency ω decreases more (but still within 5%) with increasing β_{hot}, i.e., the spectrum of the unstable TAE shifts toward the lower continuum branch. This observation is consistent with the results shown in Ref. 15. Compared to simulations with kinetic thermal ions, the mode linear growth rate is higher and the mode frequency is lower. However, the scaling tread obtained from these models is consistent. The enhancement in the mode real frequency is not from the effective MHD inertia because the Alfvén speed is much larger than the ion thermal speed. The increase in the linear growth rate in the reduced model is expected because the ion Landau damping[31,32] and the damping from electron pressure term are included in the kinetic model. We can roughly estimate the thermal ion Landau damping according to the formula in Refs. 31 and 32 and we obtain $\gamma_{\text{id}}/\omega \sim 0.08\%$, which is very small compared to the simulation results. So we expect that the main damping effect here is from electron pressure term. In addition, from Fig. 12 we can see that the energetic particle FLR effects can reduce the mode instability.

V. KINETIC DAMPING EFFECTS OF TAES

Two main damping mechanisms can be induced by thermal ions: thermal ion Landau damping and kinetic radiative damping. In our parameter regime, thermal ion Landau damping is not the dominant one, so our study focuses on radiative damping caused by thermal ion FLR effects. To resolve kinetic effects from short wavelength modes, the quasineutrality condition in the long wavelength limit [Eq.

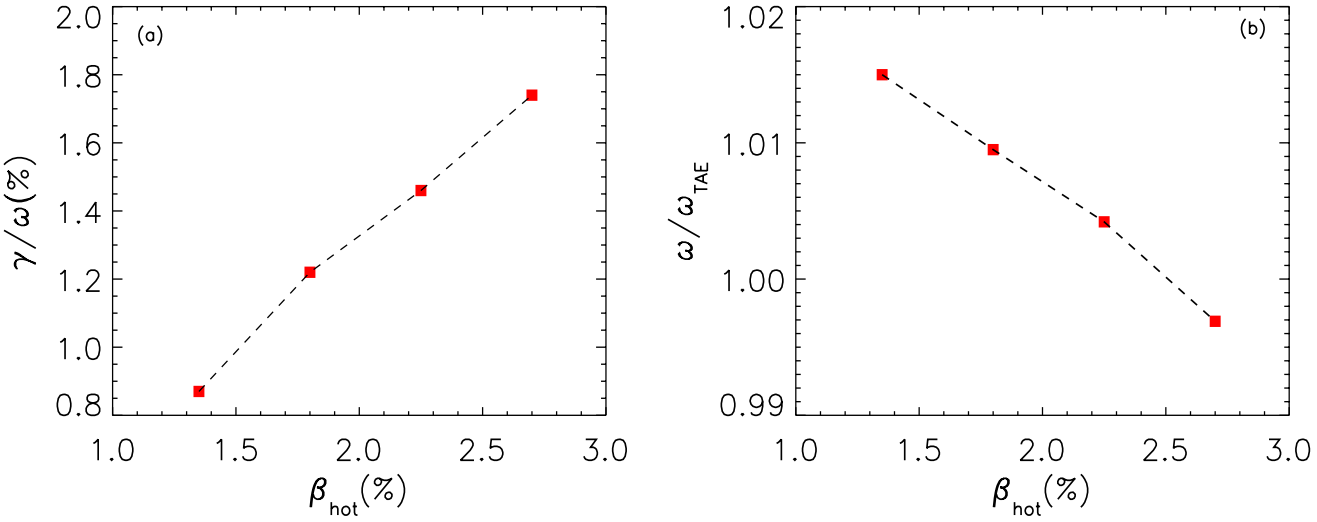

FIG. 10. (Color online) (a) The mode growth vs the central energetic particle pressure. (b) The mode frequency vs central energetic particle pressure. This is from simulations with kinetic energetic particles and thermal ions.

(14)] is no longer accurate, which should be replaced by the original gyrokinetic Poisson equation in which high-order FLR effects are included. Such high-order thermal ion FLR effects will cause radiative damping of TAEs due to the coupling to KAWs.[23,24] In Ref. 33, numerical simulations containing fourth-order kinetic term have demonstrated the radiative damping, where series expansion assuming small thermal ion gyroradius is employed in the kinetic operator. Here, we will explore the damping effect using the fully gyrokinetic operator.

A. Theory prediction of radiative damping

For a single TAE localized at the $q=q_m$ magnetic flux surface where $q_m=(m+\frac{1}{2})/n$, the radiative damping from the core thermal ions can be evaluated as follows:[24,34]

$$\frac{\gamma_d}{\omega_0}=\frac{1}{2}\hat{\epsilon}\frac{\omega^2}{\omega_0^2}\sqrt{(1-h_m)^3}\delta\alpha_m. \tag{19}$$

Here, the effective aspect ratio is defined as $\hat{\epsilon}=2r_m/R_0$ in the absence of the Shafranov shift,[24,33] r_m is the mode radial location $q_m=q(r_m)$, ω is the mode frequency which is estimated from our reduced model simulations, ω_0 is the ideal TAE mode frequency which is estimated by the continuum gap boundary $\omega_0^2=\frac{1}{2}(\omega_L^2+\omega_U^2)$, h_m is determined by the real TAE frequency, the ideal TAE frequency, and the effective aspect ratio

$$h_m=\frac{1}{\hat{\epsilon}}\left(\frac{\omega^2}{\omega_0^2}-1\right), \tag{20}$$

and $\delta\alpha_m$ is given by

$$\alpha_m=-\frac{i}{\sqrt{(1-h_m^2)}}\exp\left[-\frac{2}{\eta_m}I_1(h_m)\right], \tag{21}$$

where

$$I_1=-\int_0^{\sqrt{(1+h_m)}}dx\sqrt{1-(h_m-x^2)^2} \tag{22}$$

and

$$\eta_m=8n^2\hat{s}^2q_m^2\frac{\rho_s^2}{\hat{\epsilon}^3r_m^2}, \tag{23}$$

where the effective gyroradius is estimated by $\rho_s=\rho_i\sqrt{3/4}$ and the ion gyroradius is $\rho_i=\sqrt{2T_i/m_i}$. The damping effect from the parallel electric field (derived from the parallel electron pressure gradient) is not implied in this formula. The radiative damping has been demonstrated in a "reduced kinetic" simulation.[33] In Sec. V B, we will simulate the damping effect with Eq. (10).

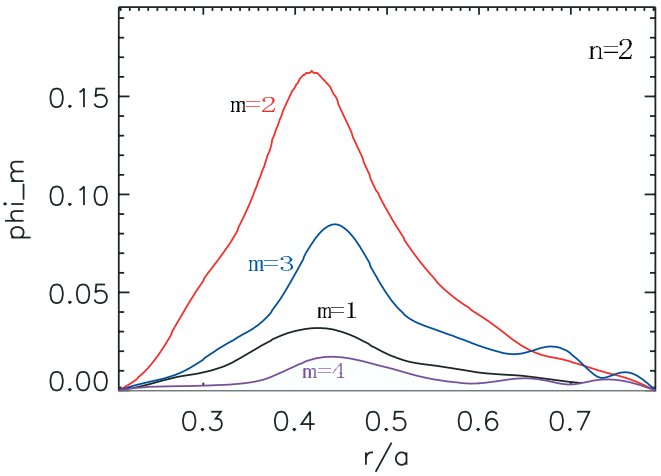

FIG. 11. (Color online) Radial profile of different poloidal harmonics for the $n=2$ mode in the presence of energetic particle drive; from top to bottom, the first line is for $m=2$, the second line is for $m=3$, the third line is for $m=1$, and the fourth line is for $m=4$. This is from the reduced model where energetic particles are fully gyrokinetic but background plasmas are treated using the fluid model.

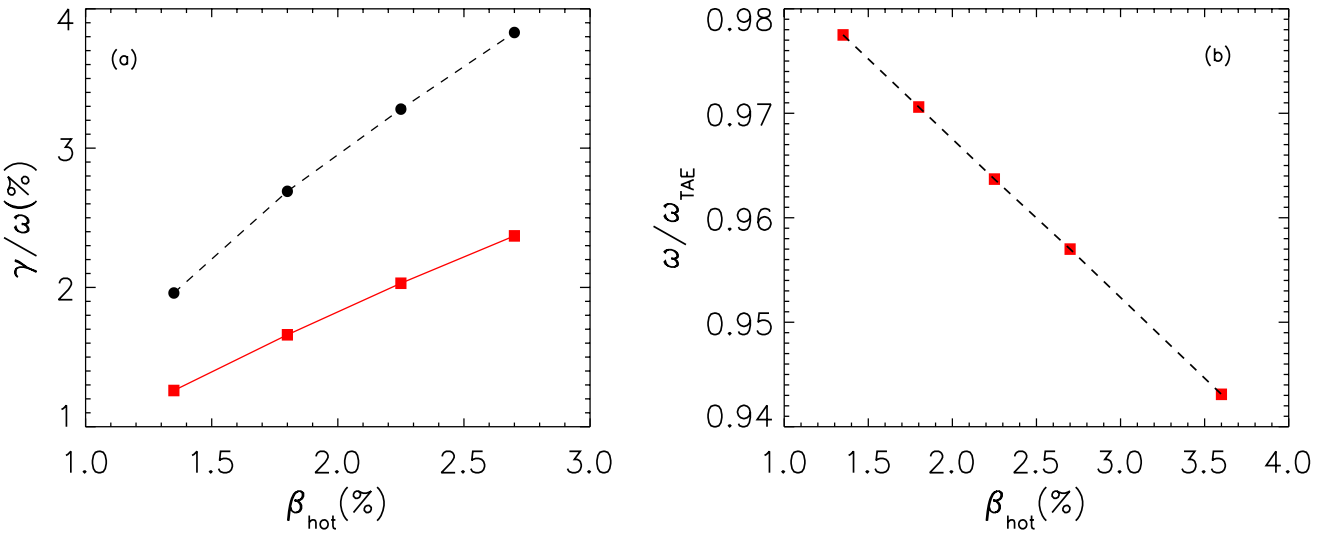

FIG. 12. (Color online) (a) The mode growth vs the energetic particle pressure. The black circles indicate the growth rate without the energetic particle FLR effect, and the red squares indicate the growth rate with the energetic particle FLR effect. (b) The mode frequency vs energetic particle pressure. This is from reduced model simulations.

The damping rate is extremely sensitive to the value of h_m so we should be very careful in estimating the mode frequency. We can estimate the continuum boundary ω_L and ω_U through the analytical formula [through Eq. (17)] or the eigenmode solutions mentioned in Sec. III A. These two results agree pretty well (within 1%) on the lower continuum boundary, which is the most sensitive parameter to determine the damping rate. Using the TAE frequency obtained from the reduced simulations, the lower continuum boundary from eigenmode calculation, and the upper continuum boundary from Eq. (17), we can obtain the analytical radiative damping rate.

B. Simulation results

We now replace the long wavelength limit gyrokinetic Poisson equation [Eq. (14)] with the conventional gyrokinetic Poisson equation [Eq. (10)] to study the kinetic "radiative damping." For simplicity, we apply reduced model for background plasmas, that is, Eqs. (12) and (13). In Eq. (10), small gyroradius assumption is not used and it contains all high-order kinetic physics. In our simulations, we do not consider the kinetic effects of electrons so their damping effect is neglected.

To accurately measure the damping rate due to the FLR effects contained in Eq. (10), we run identical simulations, both include energetic particles to drive the $n=2$ mode unstable, but one uses Eq. (14) and the other one uses Eq. (10). When Eq. (10) is used, the finite radial KAW mode structure caused by kinetic effects is observed, as in Fig. 13, which shows the kinetic wave feature in the electric potential mode structure of different poloidal harmonics m's with toroidal number $n=2$, where the thermal ion gyroradius is $\rho_i/a=0.55\%$. We estimate the damping effect by subtracting the mode growth rate obtained from gyrokinetic Poisson solver [Eq. (10)] from the growth rate obtained from solving Eq. (14). The damping rate increases with the thermal ion temperature, as expected according to theory.[24,33] The scaling between the damping rate and the thermal ion gyroradius is obtained, as shown in Fig. 14. This result shows reasonable agreement between simulations and theory. In analytical calculation, series expansion based on small thermal ion gyroradius is implied in the derivation of the gyrokinetic operator, where up to the fourth-order of $k_\perp \rho_i$ is retained, whereas all high-order nonlinear terms are included in the gyrokinetic Poisson solver. These high-order terms could be important for parameter regimes with high thermal ion temperature which corresponds to larger thermal ion gyroradius. This could explain that the discrepancy between theory and simulation becomes bigger as ρ_i/a increases. When ρ_i is very small where little damping is expected, statistical error will limit the accuracy in numerical measurement.

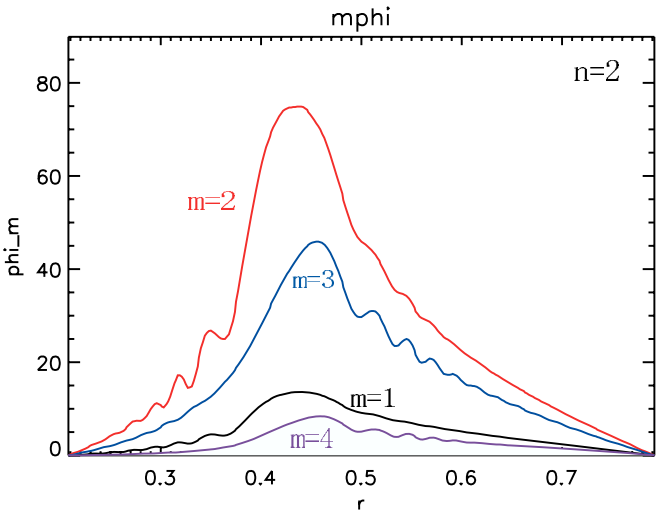

FIG. 13. (Color online) Radial profile of different poloidal harmonics for the $n=2$ mode in the presence of high-order kinetic effects; from top to bottom, the first line is for $m=2$, the second line is for $m=3$, the third line is for $m=1$, and the fourth line is for $m=4$. The radial finite structure indicates KAWs.

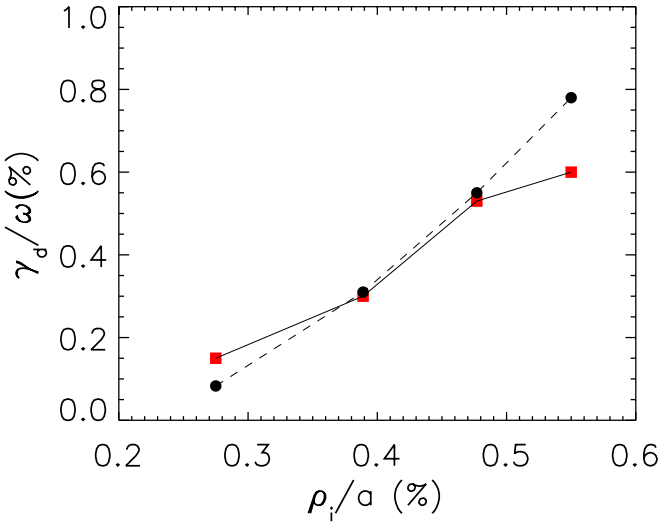

FIG. 14. (Color online) Comparison between theoretical calculation and simulations for the kinetic damping rate at different thermal ion gyroradii. The dashed line is from theory and the solid line is from simulation.

VI. SUMMARY

In summary, the properties of a discrete TAE have been investigated using a global gyrokinetic δf code. We have implemented the massless fluid electron model in the GEM code. Using a low-n TAE test case, we observe the existence of a global discrete eigenmode in the simulations. This observed mode frequency is within the continuum spectrum gap and is close to the lower continuum frequency, which agrees well with the theoretical prediction. We develop an eigenmode analysis for the reduced model, which shows very good agreement with simulation results in both the mode frequency and the mode structure. We have also demonstrated the destabilization of TAEs by energetic particles. Of particular interest is that radiative damping due to the core thermal ions is demonstrated for the first time in a nonperturbative gyrokinetic simulation. By varying the thermal ion temperature, the scaling between the radiative damping rate and the thermal ion gyroradius is quantitatively studied. The scaling obtained in simulations shows a reasonable agreement with that obtained in the analytical calculation.

Compared to previous gyrokinetic particle simulations,[14–16] similar gyrokinetic PIC method is applied in this work. In Refs. 14 and 15, electrons are taken into account through a fluid model and TAEs are destabilized by energetic particles in the absence of kinetic thermal ions, where the transition from TAE to EPM is observed. In our corresponding studies (Fig. 12), similar trend is found in the scaling of both growth rate and frequency versus energetic particle pressure. In Ref. 16, both thermal ions and electrons are treated kinetically, which includes the kinetic effects of thermal ions as well as of electrons. Their fully kinetic simulations have shown very good agreement with an ideal MHD code in the TAE mode frequency and mode structure. However, the high-order thermal ion FLR effects are not retained in their simulations. Here, we carefully benchmarked our simulation results to the eigenmode analysis based our simulation model as well as analytical calculations.[2,24] The driving effect of energetic particles is investigated together with kinetic thermal ions, where kinetic damping effect from the background plasmas is observed. Particularly, we study the kinetic radiative damping using the fully gyrokinetic operator and compare it with analytical theory. As future work, it becomes feasible for GEM to study the Alfvénic mode excitation by the ion temperature gradient and the interaction between turbulence and TAEs with fully gyrokinetic thermal ions.

ACKNOWLEDGMENTS

We thank Dr. Nikolai Gorelenkov and Dr. T. S. Hahm for helpful discussions.

This work was supported by the Department of Energy's Scientific Discovery through Advanced Computing Program, "Center for Extended Magnetohydrodynamic Modeling," and by the U.S. Department of Energy under Grant No. DE-AC02-09-CH11466.

APPENDIX: EIGENMODE ANALYSIS

In this appendix we will introduce our eigenmode calculation. Based on the TAE eigenmode equation [Eq. (15)], we can compute the frequency and the electric potential by discretizing, which will turn the problem into finding the eigenvalues and the corresponding eigenfunctions of a matrix. In principle, the matrix should be 3D because the electrostatic potential is a function of all coordinates. However, we know that the toroidal mode number n is a good quantum number in Fourier decomposition. The toroidal mode number n corresponds to the wavenumber k_y in field-line-following coordinates.[35] We can do a Fourier transform of Eq. (15) along the toroidal direction ($\mathbf{y}$) and keep only one k_y mode. Taking the Fourier transform in the toroidal direction, the 3D operator

$$\nabla = \nabla x \frac{\partial}{\partial x} + \nabla y \frac{\partial}{\partial y} + \nabla z \frac{\partial}{\partial z} \tag{A1}$$

becomes

$$\nabla = \nabla x \frac{\partial}{\partial x} + ik_y \nabla y + \nabla z \frac{\partial}{\partial z}. \tag{A2}$$

Thus, the matrix is reduced to two dimensions (x,z). After replacing $\partial^2/\partial t^2$ with $-\omega^2$, the left-hand side of Eq. (15) is given in k_y phase space

$$\frac{\partial^2}{\partial t} \nabla \cdot \frac{1}{V_A(r)^2} \nabla_\perp \delta\phi = -\omega^2 \left(\nabla x \frac{\partial}{\partial x} + ik_y \nabla y + \nabla z \frac{\partial}{\partial z} \right) \frac{1}{V_A(x,z)^2} \times \left(\nabla x \frac{\partial}{\partial x} + ik_y \nabla y \right) \delta\phi. \tag{A3}$$

In the right-hand side of Eq. (15), the form $\mathbf{b}\cdot\nabla$ relates to $\partial/\partial z$ by a factor $q_0 R_0 \Psi |\nabla r \times \nabla \theta| / RBJ$, where Ψ is the poloidal flux function and J is calculated from the

Jacobian coefficient. The factor J depends on (x,z) and is close to unity. For the sake of numerical simplicity, we make approximations

$$\mathbf{B}\cdot\nabla\frac{(\delta u_{\parallel i}-\delta u_{\parallel e})}{B}=\mathbf{b}\cdot\nabla(\delta u_{\parallel i}-\delta u_{\parallel e}),$$

$$\mathbf{b}\cdot\nabla=\frac{\partial}{\partial z}. \tag{A4}$$

This reduces the right-hand side to

$$\mathbf{B}\cdot\nabla\frac{1}{B}\nabla_{\perp}^{2}\mathbf{b}\cdot\nabla\delta\phi=\frac{\partial}{\partial z}\nabla_{\perp}^{2}\frac{\partial}{\partial z}\delta\phi. \tag{A5}$$

Notice that $\partial/\partial z$ must act on the operator $\nabla_{\perp}^{2}$ because it is not constant along the **z** direction. In the field-line-following coordinates, the right-hand term of Eq. (A5) is analytically expressed as

$$\frac{\partial}{\partial z}\nabla_{\perp}^{2}\frac{\partial}{\partial z}\delta\phi=\frac{\partial}{\partial z}\left[\frac{\partial^{3}}{\partial x^{2}\,\partial z}+2ik_{y}\nabla x\cdot\nabla y\frac{\partial^{2}}{\partial x\,\partial z}-k_{y}^{2}\nabla y^{2}\frac{\partial}{\partial z}+\nabla^{2}x\frac{\partial^{2}}{\partial x\,\partial z}+ik_{y}\nabla^{2}y\frac{\partial}{\partial z}\right]\delta\phi. \tag{A6}$$

This approximation greatly simplifies the analytical derivation, which would otherwise add hundred more terms. For the comparison, we can still get the correct conclusion as long as the same approximations are made in both the eigenmode analysis and simulations.

To numerically solve the eigenequation, partial differential operators in (x,z) are replaced by finite differences on grids such as

$$\frac{\partial\delta\phi(x_j,k_y,z_k)}{\partial x}=\frac{\delta\phi(x_{j+1},k_y,z_k)-\delta\phi(x_{j-1},k_y,z_k)}{2dx},$$

$$\frac{\partial\delta\phi(x_j,k_y,z_k)}{\partial z}=\frac{\delta\phi(x_j,k_y,z_{k+1})-\delta\phi(x_j,k_y,z_{k-1})}{2dz},$$

$$\frac{\partial B(x_j,z_k)}{\partial x}=\frac{B(x_{j+1},z_k)-B(x_{j-1},z_k)}{2dx}, \tag{A7}$$

$$\frac{\partial B(x_j,z_k)}{\partial z}=\frac{B(x_j,z_{k+1})-B(x_j,z_{k-1})}{2dz},$$

$$\nabla^{2}x=\left(\nabla x\frac{\partial}{\partial x}+ik_{y}\nabla y+\nabla z\frac{\partial}{\partial z}\right)\cdot\nabla x,$$

where dx and dz are grid sizes along the **x** and **z** directions. The grid sizes are defined in the same way as those in the flux-tube code $dx=L_x/N_x$ and $dz=L_z/N_z$. Here, L_x and L_z are the simulation lengths, and N_x and N_z are the number of grid cells per length. Quantities such as $|\nabla x|^2$, $|\nabla y|^2$, $\nabla^2 x$, and $\partial B/\partial x$ are functions of the real position and are evaluated from Miller equilibrium profiles in simulations. Numerically, the left-hand side term of Eq. (15) can be further represented in matrix form M_L. The matrix is based on the 9-point stencil form of the left-hand side operator, which is straightforward to derive, but the process is loaded down with trivial details.

In simulations, zero-boundary conditions are applied for the electrostatic potential in the radial direction (**x**) and periodic boundary conditions are applied in the field-line direction (**z**). This reduces the number of unknown $\delta\phi$ components from $(N_x+1)\times(N_z+1)$ to $(N_x-1)\times N_z$. In k_y phase space, the periodic boundary condition along the field-line direction is more complicated compared to that in real space. We need to consider the toroidal mapping effect from the initial position (x_j,y_0,z_0) to the ending position (x_j,y_{N_y},z_{N_z}), which brings a factor difference of $e^{ik_y\Delta y}$ between $\delta\phi(x_j,k_y,z_{N_z})$ and $\delta\phi(x_j,k_y,z_0)$. Here $\Delta y=2\pi q(r)r_0/q_0$ is the distance one moves along the toroidal direction (**y**) when z moves from z_0 to z_{N_z}.

Following the same procedure, we can build up the matrix of the right-hand side of Eq. (A5). Partial differential operators and quantities are computed in the same way as the left-hand side. The right-hand side matrix is labeled as M_R and its 9-point stencil form is derived from the finite difference method as well. Now Eq. (A5) can be written in the matrix form

$$-\omega^{2}M_{L}\delta\phi=M_{R}\delta\phi. \tag{A8}$$

The determinant of the matrix M_L is nonzero, so its inverse matrix M_L^{-1} exists. Multiplying M_L^{-1} on both sides, we can just solve for the eigenvalue and eigenfunction of the matrix in order to obtain ω and $\delta\phi$ from Eq. (A8). Now the matrix equation is

$$M_{L}^{-1}\times M_{R}\delta\phi=-\omega^{2}\delta\phi. \tag{A9}$$

We have checked the effect of the simplifications $\mathbf{B}\cdot\nabla(\delta u_{\parallel i}-\delta u_{\parallel e})/B=\mathbf{b}\cdot\nabla(\delta u_{\parallel i}-\delta u_{\parallel e})$ and $\mathbf{b}\cdot\nabla=\partial/\partial z$ made in simulations and eigenmode calculation. Simulating the original equations shown in Sec. III, we still obtain the TAE with the electric potential contour plot, which is very close to the contour plot obtained from the simplified simulations. The variation in frequency is within 1% of the simplified form. These observations show convincingly that the observed $n=2$ mode is the theoretically predicted TAE eigenmode.

In the eigenmode analysis, we use the library LAPACK to compute the inverse matrix M_L^{-1} and solve for eigenvalues and eigenfunctions of matrix $M_L^{-1}\times M_R$. The file names of these two computations are individually ZGETRI.f and ZGEEV.f. For a 4096×4096 matrix $(N_x=128,N_z=32)$, it takes one processor of the NERSC Cray XT4 system (named Franklin) about 3 h to finish the computation and output all eigenvalues and eigenfunctions.

[1] C. Z. Cheng and M. S. Chance, Phys. Fluids **29**, 3695 (1986).
[2] G. Y. Fu and J. W. Van Dam, Phys. Fluids B **1**, 1949 (1989); G. Y. Fu, Ph.D. thesis, University of Texas, 1988.
[3] L. Chen, in *Proceedings of the Joint Varenna Lausanne International Workshop*, Chexbres, Switzerland, 3–7 October 1988, edited by J. Vaclavik, F. Troyon, and E. Sindoni (Societa Italiana di Fisica by Editrice Compositori, Bologna, 1988), p. 327.
[4] L. Chen, Phys. Plasmas **1**, 1519 (1994).
[5] F. Zonca and L. Chen, Phys. Plasmas **3**, 323 (1996).
[6] C. Z. Cheng, N. N. Gorelenkov, and C. T. Hsu, Nucl. Fusion **35**, 1639 (1995).
[7] W. Park, S. Parker, H. Biglari, M. Chance, L. Chen, C. Z. Cheng, T. S.

Hahm, W. W. Lee, R. Kulsrud, D. Monticello, L. Sugiyama, and R. White, Phys. Fluids B **4**, 2033 (1992).
[8]G. Y. Fu and W. Park, Phys. Rev. Lett. **74**, 1594 (1995).
[9]S. Briguglio, G. Vlad, F. Zonka, and C. Kar, Phys. Plasmas **2**, 3711 (1995).
[10]Y. Todo and T. Sato, Phys. Plasmas **5**, 1321 (1998).
[11]F. Zonca, L. Chen, R. A. Santoro, and J. Q. Dong, Plasma Phys. Controlled Fusion **40**, 2009 (1998).
[12]P. Lauber, S. Gunter, and S. D. Pinches, Phys. Plasmas **12**, 122501 (2005).
[13]P. Lauber, S. Gnter, A. Knies, and S. D. Pinches, J. Comput. Phys. **226**, 447 (2007).
[14]Y. Nishimura, Z. Lin, and W. X. Wang, Phys. Plasmas **14**, 042503 (2007).
[15]Y. Nishimura, Phys. Plasmas **16**, 030702 (2009).
[16]A. Mishchenko, R. Hatzky, and A. Könies, Phys. Plasmas **15**, 112106 (2008).
[17]H. Qin, W. M. Tang, and G. Rewoldt, Phys. Plasmas **5**, 1035 (1998).
[18]H. Qin, W. M. Tang, and G. Rewoldt, Phys. Plasmas **6**, 2544 (1999).
[19]Y. Chen and S. E. Parker, J. Comput. Phys. **189**, 463 (2003).
[20]Y. Chen and S. E. Parker, J. Comput. Phys. **220**, 839 (2007).
[21]J. Cummings, Ph.D. thesis, Princeton University, 1994.
[22]Y. Chen and S. Parker, Phys. Plasmas **8**, 441 (2001).
[23]R. R. Mett and S. M. Mahajan, Phys. Fluids B **4**, 2885 (1992).
[24]H. L. Berk, R. R. Mett, and D. M. Lindberg, Phys. Fluids B **5**, 3969 (1993).
[25]A. Hasegawa and L. Chen, Phys. Rev. Lett. **32**, 454 (1974).
[26]W. W. Lee, J. Comput. Phys. **72**, 243 (1987).
[27]R. L. Miller, M. S. Chu, J. M. Greene, Y. R. Lin-Liu, and R. E. Waltz, Phys. Plasmas **5**, 973 (1998).
[28]C. E. Kieras and J. A. Tataronis, J. Plasma Phys. **28**, 395 (1982).
[29]C. Z. Cheng, L. Chen, and M. S. Chance, Ann. Phys. (N.Y.) **161**, 21 (1985).
[30]S. Briguglio, F. Zonca, and G. Vlad, Phys. Plasmas **5**, 3287 (1998).
[31]R. Betti and J. P. Freidberg, Phys. Fluids B **3**, 1865 (1991).
[32]C. Z. Cheng, Phys. Fluids B **3**, 2463 (1991).
[33]G. Y. Fu, H. L. Berk, and A. Pletzer, Phys. Plasmas **12**, 082505 (2005).
[34]G. Y. Fu, C. Z. Cheng, R. Budny, Z. Chang, D. S. Darrow, E. Fredrickson, E. Mazzucato, R. Nazikian, K. L. Wong, and S. Zweben, Phys. Plasmas **3**, 4036 (1996).
[35]M. A. Beer, S. C. Cowley, and G. W. Hammett, Phys. Plasmas **2**, 2687 (1995).